ARTICLE | OPEN ACCESS

Drug Discovery

To Cite:
Osasan SA, Ambrose GO, Daramola O, Adefolalu OA, Hind AA, Jawaher MA, Ibrahim WO, Ajetunmobi OI. Ensemble docking and molecular dynamics validation of quinazoline c9 targeting mutant kras(g12c). *Drug Discovery* 2026; 20: e17dd3099
doi:

Author Affiliation:
[1]Department of Laboratory Medicine, Ministry of Health (Prince Mishari Bin Saud Hospital, Baljurashi, Al-Baha), Kingdom of Saudi Arabia
[2]University of Ilorin Teaching Hospital, Ilorin, Nigeria
[3]North Devon District Hospital, Barnstaple, United Kingdom
[4]Obafemi Awolowo University Teaching Hospital, Ile-Ife, Osun State, Nigeria
[5]Department of Basic Science, College of Applied Medical Sciences, University of Al-Baha, Al-Baha, Saudi Arabia
[6]Optometry Department, Faculty of Applied Medical Sciences, Al-Baha University, Al-Baha, Saudi Arabia
[7]Saudi Arabia Board of Preventive Medicine, Al-Baha, Saudi Arabia
[8]Department of Histopathology, University Hospitals Morecambe Bay, NHS Trust, Kendal, United Kingdom
† Co-First Authors

***Corresponding Author:**
Osasan Stephen Adebayo,
Department of Laboratory Medicine, Ministry of Health, Prince Mishari Bin Saud Hospital, Baljurashi, Al-Baha, Saudi Arabia,
ORCID iD: https://orcid.org/0009-0006-2718-8965,
Email: stephenosasan2@gmail.com sosasan@moh.gov.sa, stephenosasan@yahoo.com
Ph: - +966509790614

Peer-Review History
Received: 29 November 2025
Reviewed & Revised: 12/December/2025 to 15/July/2026
Accepted: 29 July 2026
Published: 18 August 2026

Peer-Review Model
External peer-review was done through double-blind method.

Drug Discovery
pISSN 2278–540X; eISSN 2278–5396

Ensemble docking and molecular dynamics validation of quinazoline c9 targeting mutant kras(g12c)

Stephen Adebayo Osasan[1,7†*], George Oche Ambrose[2†], Olusola Daramola[3], Oluwafemi Ayodele Adefolalu[4], Alzahrani A. Hind[5], Mohammad Alshehri Jawaher[6], Wisdom Onuche Ibrahim[2], Olanrewaju I Ajetunmobi[8]

ABSTRACT

The KRAS(G12C) mutations represent a major oncogenic driver in multiple types of cancer. Covalent inhibitors such as sotorasib have shown clinical efficacy, but identifying alternative scaffolds that can stabilise the Switch-II pocket remains an important goal in targeted drug discovery. In this study, combined docking analyses of two crystal structures, 7O70 and 7O83, were performed, and it was observed that C9 has better binding affinity (-7.0 and -8.0 kcal/mol) than sotorasib (-5.4 and -6.6 kcal/mol) and can attain good ligand recognition in different conformations. The interaction network analysis showed that C9 interacts with key residues in the Switch-II pocket, such as CYS12, GLU62, ARG68, ASP69, ASP92, MET72, HIS95 and TYR96, via complementary electrostatic, aromatic and hydrophobic interactions. Importantly, the mutant residue CYS12 and aromatic stacking with TYR96 could stabilise the ligand in a stable state by π-sulfur contacts. Molecular dynamics simulations (100 ns) showed the complexes to be stable. The RMSD trajectories suggested stable protein backbones and ligand poses, with the C9 complexes showing lower ligand RMSD values than the control in the 7O70 system. Furthermore, the radius of gyration analysis suggested that KRAS remained globally compact during the simulations. Energetic decomposition of ligand-protein interaction energies showed that van der Waals interactions were the main contributors to the binding stabilisation. Consistently negative interaction energies were observed for the C9 complexes, especially in the 7O70 system. Taken together, these results indicate that the quinazoline compound C9 makes stable contacts in the KRAS(G12C) binding pocket, and may be a favourable scaffold for the development of next-generation KRAS(G12C) inhibitors.

Keywords: KRAS(G12C), Quinazoline C9, Molecular docking, Molecular dynamics simulation, Switch-II pocket, Targeted cancer therapy

1. INTRODUCTION

Mutations in the Kirsten rat sarcoma viral oncogene homolog (KRAS) are among the most common oncogenic alterations in human cancers and play a particularly

important role in non-small cell lung cancer (NSCLC), pancreatic ductal adenocarcinoma, and colorectal cancer. Lung cancer is the leading cause of cancer-related death worldwide, with about 1.8 million deaths per year. One of the most common molecular drivers of this malignant tumour type is KRAS mutations (Sung et al., 2021). These mutations promote the constitutive activation of KRAS signalling pathways that lead to uncontrolled cell proliferation, metabolic reprogramming, and resistance to apoptosis (Pylayeva-Gupta et al., 2011). KRAS has several variants, but the G12C variant is particularly important because it replaces glycine at codon 12 with cysteine. This nucleophilic residue can be chemically targeted in the Switch-II pocket of the protein (Westover et al., 2016).

KRAS has long been considered an "undruggable" target due to its high affinity for guanosine triphosphate (GTP) and the absence of apparent druggable pockets on its surface (Cox et al., 2014). However, recent advances in structural and chemical biology have identified transient pockets in proximity to the Switch-II region that can be exploited for selective inhibition of KRAS(G12C) (Ostrem et al., 2013). This breakthrough opened the door to the development of covalent inhibitors such as sotorasib (AMG-510) and adagrasib that covalently bind to the mutant cysteine residue and lock KRAS in an inactive GDP-bound state (Lanman et al., 2020). These drugs represent a breakthrough in the field of targeted cancer therapy; however, resistance mechanisms and limited activity in specific tumour contexts emphasise the need to investigate new scaffolds and alternative inhibitor chemotypes that can stabilise the KRAS(G12C) pocket through different interaction mechanisms (Canon et al., 2019).

Computational methods are the core tools supporting modern drug research and development, as they can complete the identification and optimisation of candidate molecules before experimental verification; Quantitative Structure-Activity Relationship (QSAR) modelling, the core technology of this field, links molecular descriptors to biological activity and guides the design of new inhibitors (Tropsha, 2010). By combining statistical learning methods with descriptor-based modelling, QSAR frameworks can predict the potency of untested compounds and accelerate lead discovery (Cherkasov et al., 2014). The performance and interpretability of QSAR-based drug discovery pipelines have been improved by further development of machine learning algorithms like regression optimised by a genetic algorithm and ensemble learning (Todeschini & Consonni, 2009).

We have previously reported on the application of an integrated QSAR modelling and de novo design workflow to identify novel KRAS inhibitor candidates from a set of experimentally characterised compounds. The most promising hit was a quinazoline derivative, C9, selected by virtual screening of newly generated molecules guided by machine learning, with predicted inhibitory potency ($pIC_{50} \approx 8.11$) and drug-likeness and toxicity profiles comparable with reference inhibitors (Stephen Adebayo et al., 2025). Structural analysis revealed that C9 contains a conserved quinazoline scaffold similar to existing KRAS inhibitors, but also modifications that could increase potency and reduce predicted toxicity. The QSAR framework gave strong predictive evidence of the potential activity of C9, but structure-based validation using molecular docking and molecular dynamics simulations is necessary to further characterise its binding stability and interaction dynamics inside KRAS(G12C).

The present study is a subsequent structural validation study of a hit compound, C9, targeting KRAS(G12C), identified in the previous QSAR screening study. In the present study, we will perform two main tasks using molecular docking and molecular dynamics simulations: Elucidation of the molecular mechanism of C9 binding to the Switch-II pocket and assessment of the drug-development potential of its chemical scaffold.

2. MATERIALS AND METHODS

2.1 Study design

This work was designed as a structure-based follow-up study to validate the binding behaviour of the previously reported quinazoline hit C9, which was identified by the same authors as the most promising de novo KRAS inhibitor candidate from a QSAR-guided virtual screening workflow with a predicted pIC50 of 8.11 and favourable in silico drug-likeness properties (Stephen Adebayo et al., 2025). The present study employed ensemble molecular docking and molecular dynamics (MD) simulations to investigate the binding stability, interaction profiles and dynamic behaviour of C9 in mutant KRAS(G12C) in different crystallographic conformations. The approved KRAS(G12C) inhibitor Sotorasib was used as the reference control ligand in the comparative analysis.

2.2 Protein structure retrieval and preparation

The aim of this study was to capture the conformational variability of the Switch-II pocket of KRAS(G12C). Ensemble docking was performed with crystal structures 7O70 and 7O83 from the Protein Data Bank database, and all pre-processing work was performed in PyMOL and BIOVIA Discovery Studio Visualiser: crystalline water and non-essential heteroatoms were removed, the protein backbone

and the mutated Cys12 residue were retained, hydrogen atoms were added, bond orders were verified, and atom types were assigned. Finally, we visually checked all residues were intact and the binding region was correctly orientated.

2.3 Ligand preparation

The test compound C9 was obtained from the authors' previously published QSAR-guided KRAS inhibitor discovery study in which it was the top-ranked quinazoline hit in the applicability domain of the predictive model (Stephen Adebayo et al., 2025). The control ligand sotorasib was synthesised in parallel for comparison. Ligand structures were converted into appropriate three-dimensional conformations, checked for valence consistency, protonated accordingly and geometry minimised before docking. Final ligand preparation for docking was done in PyRx, which converts the ligand files to PDBQT format required for AutoDock Vina.

2.4 Molecular docking

Molecular docking was carried out using AutoDock Vina, which is embedded in the PyRx platform. The preprocessed KRAS(G12C) protein structure was imported, and docking was performed for the Switch-II allosteric pocket that could be exploited by confirmed KRAS(G12C) inhibitors. A grid box was built around the Cys12 residue and its neighbouring recognition residues. Ligands C9 and sotorasib were docked individually under the same conditions, and their binding affinities were noted in kcal/mol. The best-ranked pose for each combination was chosen for further interaction analysis and molecular dynamics simulation.

2.5 Docking pose inspection and interaction analysis

The docked complexes were inspected and visualised using PyMOL and BIOVIA Discovery Studio Visualiser. Two- and three-dimensional interaction maps were generated to identify hydrogen bonds, electrostatic contacts, aromatic stacking interactions, halogen contacts, sulfur-mediated interactions and hydrophobic contacts. Residues involved in ligand binding were noted for each docked complex, and distances of interaction were noted. These docking-based interaction networks were then used to compare the binding architecture of C9 and sotorasib in the various conformations of KRAS(G12C).

2.6 Molecular dynamics simulation setup

Molecular dynamics simulations were performed on the complexes selected from the molecular docking stage using GROMACS. Each protein-ligand complex was parameterised and prepared for simulation in an explicit solvent environment. The protein topology was generated using the relevant protein force field in GROMACS. The ligand parameters were added to the system before the production simulation. Each complex was solvated in a water box, and counterions were added for neutralisation. First, the starting geometry was optimised, and steric clashes were removed by energy minimisation. The minimised systems were then equilibrated in both constant volume and constant pressure conditions before starting the production MD runs.

Production simulations were performed for each complex for 100 ns. The production outputs were considered as segmented trajectories for downstream trajectory analysis, and concatenated into a single continuous trajectory corresponding to the full simulation duration. In the analysis pipeline, ten trajectory segments were merged into one trajectory file, leading to a total of 10,000 frames, which represents 100 ns or 0.01 ns/frame.

2.7 Trajectory concatenation and post-processing

We concatenated post-simulation trajectory segments for analysis using MDTraj. Read in topology and individual production trajectory files, combine into one netCDF trajectory, and saved for consistent downstream processing. Then the concatenated trajectory was reloaded in PyTraj and MDTraj and the corresponding analysis libraries were used depending on the metric calculated. All the time-resolved analyses were performed on this single unified 100 ns trajectory.

2.8 Root mean square deviation analysis

Structural stability of each protein-ligand complex was assessed by root mean square deviation (RMSD) analysis. The RMSD of the protein Cα atoms and ligand heavy atoms were calculated using MDTraj. Prior to RMSD calculation, trajectories were aligned to the initial frame using the protein Cα atoms as the reference selection. Backbone stability was determined using protein RMSD during the simulation, and stability of the docked binding pose in the pocket of KRAS(G12C) was determined using ligand RMSD. Plots of time-resolved RMSD values as a function of simulation time were exported as comma-separated files.

2.9 Radius of gyration analysis

We evaluated global structural compactness of KRAS(G12C) during simulation by using the radius of gyration (Rg). Rg was computed from the protein atoms using MDTraj and was given in angstroms. Two types of analyses were generated: a time-resolved Rg trajectory and a distribution plot from the entire simulation. Kernel density estimation was used to visualise the distribution of Rg values along the 100 ns trajectory. These analyses were done to see if ligand binding led to expansion or destabilisation of the global fold of KRAS(G12C).

2.10 Root mean square fluctuation analysis

The residue-level flexibility was described by calculating the root mean square fluctuation (RMSF) for protein Cα atoms. All frames were first aligned on the first frame using the protein Cα atoms to remove global rotational and translational motion before performing RMSF analysis. Then RMSF values were calculated per residue and converted from nanometers to angstroms. Dynamic fluctuations were mapped along the KRAS(G12C) sequence, keeping the residue numbering of the topology file. RMSF profiles were exported as tables and plotted as a function of residue number.

2.11 Ligand–pocket distance analysis

Ligand residence time in the KRAS(G12C) binding site was monitored by distance-based analysis. Two complementary approaches were applied.

First, a general ligand-pocket distance metric was obtained by selecting all protein residues within 5.0 Å of the ligand in the first frame of the simulation. The heavy atoms of these automatically defined pocket residues were selected, and the minimum heavy-atom distance between ligand atoms and pocket atoms was calculated for each frame throughout the simulation.

In addition, we performed targeted distance analyses on some chosen mechanistic residues, specifically residues 78, 84 and 85. For these residues, the minimum heavy atom distance and centre of mass (COM) distance between the ligand and the residue set were computed as a function of time. These analyses were used to assess ligand retention, proximity to the pocket, and residue-specific anchoring behaviour during the simulation.

2.12 Ligand interaction energy analysis

Using the linear interaction energy (LIE)-style decomposition implemented in PyTraj, the time-dependent ligand-protein interaction energetics were calculated. The ligand was specified explicitly, and the rest of the system, apart from solvent molecules and ions, was considered the interacting protein environment. Distance cutoffs of 12.0 Å were used for both the electrostatic and van der Waals interaction energy terms, and the dielectric constant was set to 2.0. The total interaction energy was calculated as a sum of the electrostatic and van der Waals contributions.

To reduce the effect of extreme spikes, an interquartile range (IQR)- based outlier-filtering procedure was applied to the total, electrostatic, and van der Waals energy profiles separately. The filtered data were subsequently employed to calculate mean and standard deviation values and to plot the time-resolved plots to visualise the energetic stability of ligand binding during the 100-ns simulations.

2.13 Protein–ligand interaction fingerprint analysis

We analysed the persistent interaction patterns along the trajectories with MDAnalysis and ProLIF. The ligand was identified by residue name, and protein atoms were extracted as the receptor selection. Interaction fingerprints were calculated for the sampled snapshots along the simulation trajectory. Aggregate interaction networks were then generated with ProLIF, with resulting interaction tables exported for interpretation. Percentage of occupancy of interactions was also calculated to assess how often each type of ligand–residue interaction occurred throughout the frames sampled. This permitted the identification of the most persistent interaction edges supporting ligand binding during dynamics.

2.14 Principal component analysis

To explore large-scale conformational motions of KRAS(G12C), principal component analysis (PCA) was performed on the protein Cα atoms using PyTraj. The trajectory was fitted to the reference frame before PCA, and the first two principal components (PC1 and PC2) were extracted. Projections along PC1 and PC2 were plotted as time-colored scatter plots to visualise conformational sampling during

the simulation. In addition, kernel density plots were generated for the PC1 and PC2 distributions, and eigenvalues associated with the principal components were saved for reference.

2.15 Dynamic cross-correlation analysis

The dynamic cross-correlation matrix (DCCM) was used to evaluate atomic motions correlated within KRAS(G12C) from the Cα atoms of the protein. The concatenated trajectory was superimposed on the initial structure and the positional fluctuations around the mean structure were calculated. Pearson-type normalised cross-correlation coefficients were calculated between pairs of residues to generate residue–residue correlation maps. Positive values indicate correlated movements, and negative values indicate anti-correlated movements. The resulting cross-correlation matrices were visualised as heat maps and exported as tables in CSV format.

2.16 Data handling and statistical summarisation

All the quantities derived from the trajectory were used to generate time series from the simulation frame index converted to nanoseconds. Summary statistics (e.g., mean ± standard deviation) were computed where appropriate using scientific libraries in Python. Figures were generated using Matplotlib and numerical outputs were saved as CSV files to ensure reproducibility and for further documentation.

2.17 Software environment

AutoDock Vina in PyRx, PyMOL, and BIOVIA Discovery Studio Visualiser were used for docking and structure visualisation. Molecular dynamics simulations were performed using the GROMACS package. MDTraj, PyTraj, MDAnalysis, ProLIF, NumPy, Pandas and Matplotlib were used for trajectory processing and analysis.

3. RESULTS

3.1 Ensemble docking across KRAS(G12C) conformations

A set of KRAS(G12C) crystal structures was used to conduct ensemble docking experiments. The binding affinity of test molecule C9 in all tested conformations was superior to that of the control molecule sotorasib. Therefore, C9 was selected to carry out subsequent molecular dynamics verification (Table 1).

Table 1. Ensemble docking scores (kcal/mol) of C9 (test) and sotorasib (control) against KRAS(G12C) conformations (7O70 and 7O83).

Target (PDB ID)	Ligand (Role)	Binding affinity (kcal/mol)	RMSD/ub (Å)	RMSD/lb (Å)
7O70	Sotorasib (Control)	-5.4	0.0	0.0
7O70	C9 (Test)	-7.0	0.0	0.0
7O83	Sotorasib (Control)	-6.6	0.0	0.0
7O83	C9 (Test)	-8.0	0.0	0.0

3.2 Ligand–protein interaction networks across KRAS(G12C) conformations

Ligand-protein interaction architecture of C9 and reference inhibitor sotorasib was assessed across the 7O70 and 7O83 KRAS(G12C) crystal structures to define molecular contacts stabilising ligand binding in the Switch-II pocket. Interaction maps revealed diverse networks of electrostatic, hydrogen-bonding, aromatic and hydrophobic interactions, implying that ligand recognition is achieved by multiple complementary interaction types within the KRAS(G12C) binding cavity.

For the KRAS(G12C)–C9 complex based on the 7O70 structure, the ligand formed an extensive interaction network dominated by electrostatic and aromatic contacts. The positively polarised nitrogen atom of C9 established attractive charge interactions with GLU62 and ASP92, with distances of 3.71 Å and 4.33 Å, respectively. The additional electrostatic stabilisation was provided by π-cation interactions between the positively charged side chains of ARG68 and HIS95 and the aromatic π-system of the ligand. Complementary π–anion interactions were also detected between the ligand aromatic ring and negatively charged residues GLU62 and ASP92, which supports electrostatic complementarity inside the pocket. A unique contact was observed with the mutant residue CYS12, which formed a π–sulfur interaction with the ligand aromatic at around 4.95 Å, indicating the importance of the mutation site in ligand stabilisation.

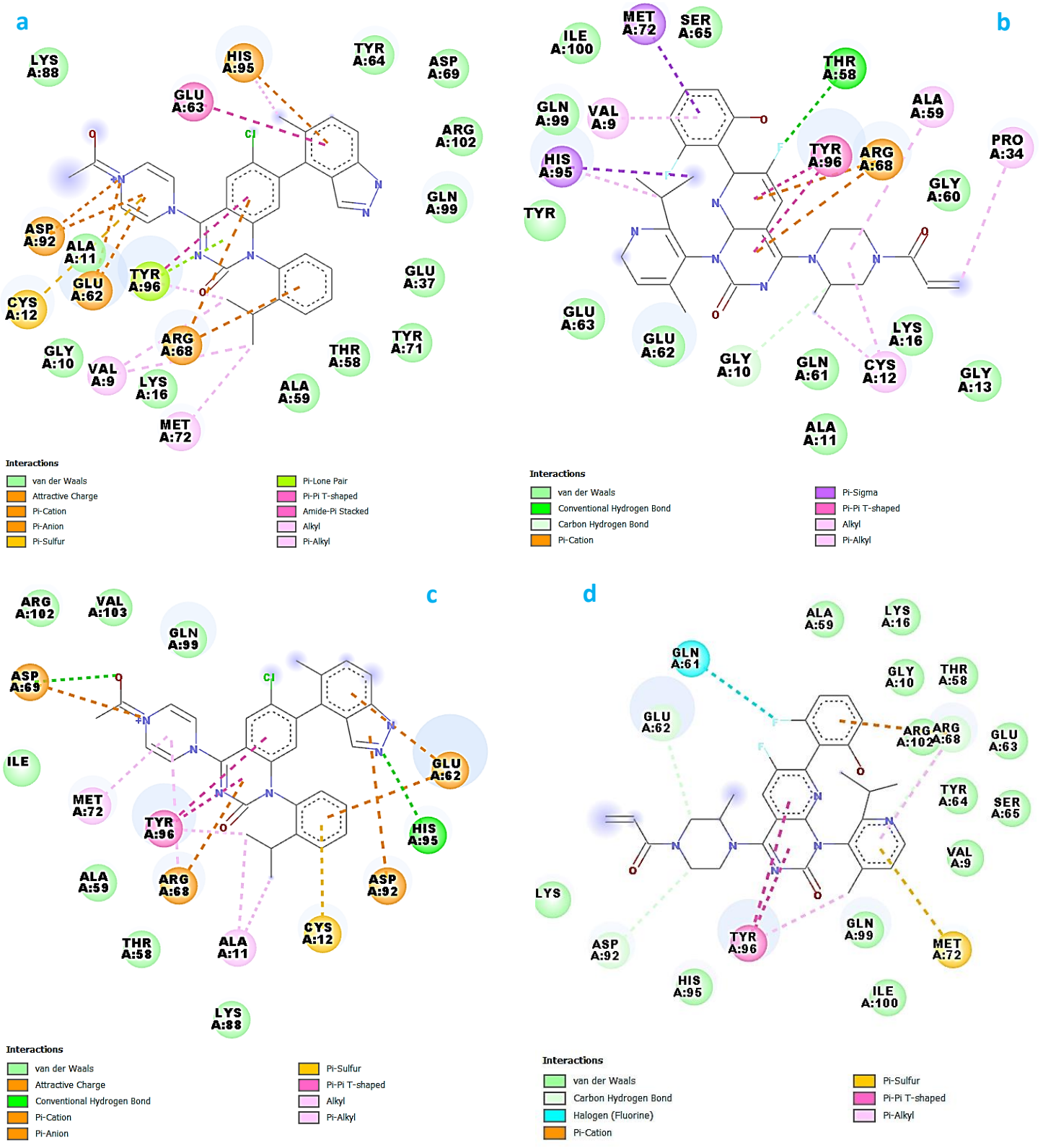

Figure 1. Ligand–protein interaction maps for KRAS(G12C) complexes. Two-dimensional interaction diagrams illustrating the nonbonded interaction networks between KRAS(G12C) and ligands across two structural conformations. (a) KRAS(G12C)–C9 complex based on the 7O70 crystal structure, showing electrostatic interactions with GLU62 and ASP92, π–cation contacts with ARG68 and HIS95, a π–sulfur interaction with CYS12, and hydrophobic contacts involving VAL9, MET72, and TYR96, (b) KRAS(G12C)–sotorasib complex based on the 7O70 structure, featuring hydrogen and halogen interactions with THR58, a carbon–hydrogen bond with GLY10, π–cation interactions with ARG68, and hydrophobic contacts with CYS12, ALA59, PRO34, and VAL9, (c) KRAS(G12C)–C9 complex based on the 7O83 structure, showing hydrogen bonds with HIS95 and ASP69, electrostatic interactions involving ARG68, GLU62, and ASP92, a π–sulfur interaction with CYS12, and aromatic stacking with TYR96 and (d) KRAS(G12C)–sotorasib complex based on the 7O83 structure, displaying hydrogen and carbon–hydrogen bond interactions with ARG68, GLU62, and ASP92, a halogen interaction with GLN61, π–cation interactions with ARG68, and aromatic stacking with TYR96.

The ligand orientation was further stabilised by aromatic packing interactions with HIS95 and TYR96 with π–π T-shaped contacts and amide–π stacking with the GLU63–TYR64 backbone. Hydrophobic contacts were also observed, with VAL9 and MET72 having alkyl interactions and HIS95, TYR96 and ARG68 involved in π–alkyl contacts; all of which support burial of the ligand within the binding pocket (Figure 1a).

In the KRAS(G12C)–sotorasib complex with 7O70, the ligand was stabilised by a combination of hydrogen bonding, electrostatic contacts, and hydrophobic interactions. One of the most important interactions was a conventional hydrogen bond between THR58 and a fluorine atom of the ligand at 2.55 Å, which also showed properties of halogen bonding. A carbon–hydrogen bond was predicted between the ligand and GLY10 (3.48 Å), which contributed to additional hydrogen-bond-like stabilisation. Electrostatic interactions included the π–cation interactions between ARG68 and the ligand aromatic ring, which contributed to the orientation of the ligand within the pocket. Moreover, we found aromatic interactions, where TYR96 made π–π T-shaped contacts and π–sigma interactions involving MET72 and HIS95 further stabilised the ligand scaffold. The hydrophobic contacts of CYS12, ALA59, PRO34, VAL9 and HIS95 further stabilised the complex by alkyl and π–alkyl interactions in the hydrophobic region of the pocket (Figure 1b).

For the complex of KRAS(G12C) with C9 extracted from the 7O83 structure, the ligand preserved a dense interaction network of hydrogen bonding, electrostatic complementarity, aromatic stacking and hydrophobic contacts. Two conventional hydrogen bonds turned out to be the main anchoring interactions, one between HIS95 and the ligand nitrogen atom (2.96 Å) and the other between a ligand oxygen atom and ASP69 (2.90 Å). An electrostatic stabilisation was also evidenced by an attractive charge interaction with ASP69, π–cation interactions with ARG68 and π–anion interactions with GLU62 and ASP92. A π–sulfur interaction with the mutant residue CYS12 (4.51 Å) was also observed, reinforcing ligand engagement within the Switch-II pocket. Aromatic stacking interactions between TYR96 and the ligand aromatic scaffold were also observed, which supported ligand orientation, and ALA11 formed alkyl contacts while ARG68, TYR96 and MET72 were involved in π–alkyl interactions, all of which contributed to the hydrophobic stabilisation within the binding cavity (Figure 1c).

The KRAS(G12C)–sotorasib complex based on the 7O83 structure also exhibited a diverse interaction profile. Among hydrogen-bonding interactions, a conventional hydrogen bond within the ligand scaffold (2.12 Å) and additional carbon–hydrogen bond interactions with ARG68, GLU62 and ASP92 were observed, which helped to maintain ligand positioning. Electrostatic complementarity was further contributed by a halogen interaction between the fluorine substituent of sotorasib and GLN61 (3.62 Å). Electrostatic stabilisation also involved π–cation interactions with ARG68, while π–sulfur interactions with MET72 contributed to aromatic stabilisation of the ligand. Aromatic stacking interactions were again observed with TYR96 forming π–π T-shaped contacts, accompanied by π–alkyl interactions involving TYR96 and ARG68, indicating hydrophobic stabilisation along the pocket surface (Figure 1d).

The interaction networks collectively demonstrate that both C9 and sotorasib interact with key residues in the KRAS(G12C) Switch-II pocket, including CYS12, GLU62, ARG68, ASP69, ASP92, MET72, HIS95, and TYR96. Ligand binding is stabilised by complementary electrostatic interactions, aromatic stacking and hydrophobic packing at the binding interfaces, which are present in multiple conformational states of KRAS(G12C).

3.3 Complex stability during molecular dynamics: RMSD analysis (protein and ligand)

The structural stability of KRAS(G12C)–ligand complexes was assessed by analysing the root mean square deviation (RMSD) of the protein Cα atoms and ligand heavy atoms over the 100-ns molecular dynamics trajectories for the 7O70 and 7O83 crystal structures. The conformational changes and the stability of the ligand pose during the simulations were monitored by calculating RMSD profiles with respect to the first frame of the simulation.

For the 7O70 structure, the protein backbone RMSD of the KRAS(G12C)–C9 complex was lower and fluctuated less during the simulation, with fluctuations mainly between 1.3 and 1.7 Å. The ligand RMSD values were relatively small, generally between 0.5 and 1.1 Å, suggesting a stable ligand conformation and consistent positioning in the binding pocket during the trajectory (Figure 2a). For the KRAS(G12C)–sotorasib complex for the 7O70 structure, the protein Cα RMSD increased in the initial stage of the trajectory and then stabilised, fluctuating mainly between approximately 2.3 and 3.1 Å for the rest of the simulation. The RMSD of the ligand fluctuated in the early stages and then stabilised with values generally in the range of 1.6-2.4 Å, indicating that the ligand retained a stable binding pose after the initial equilibration period (Figure 2b).

A similar pattern of stability was seen for the 7O83 crystal structure simulations. The protein Cα RMSD of the KRAS(G12C)–C9 complex fluctuated between 1.3 and 1.6 Å after the initial equilibration phase, whereas the ligand RMSD fluctuated between 0.8 and 1.3

Å during the simulation (Figure 2c). For the KRAS(G12C)–sotorasib complex, the protein RMSD remained stable at ~1.3–1.5 Å, while the ligand RMSD values fluctuated in the range of 0.9–1.4 Å in general (Figure 2D).

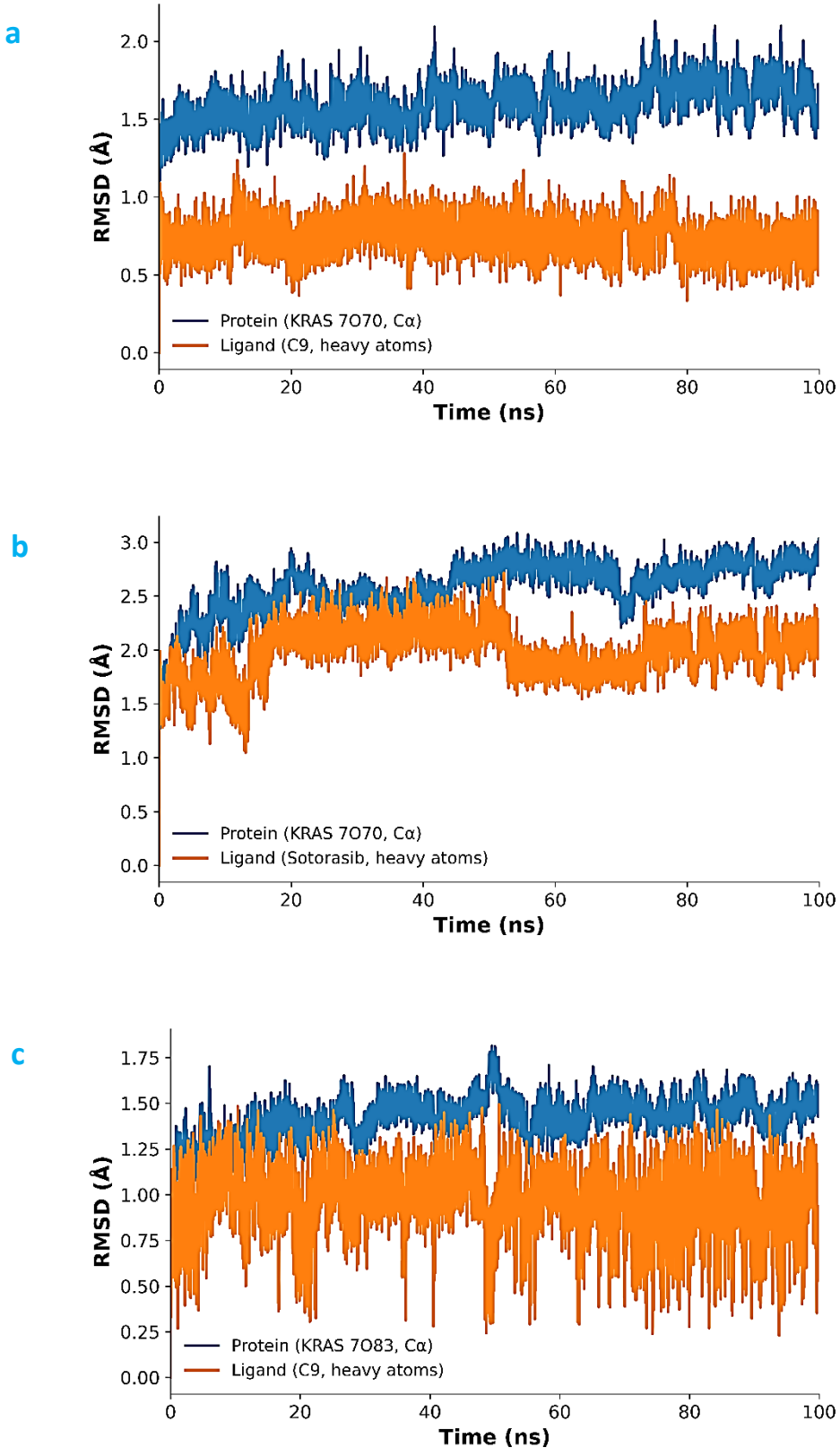

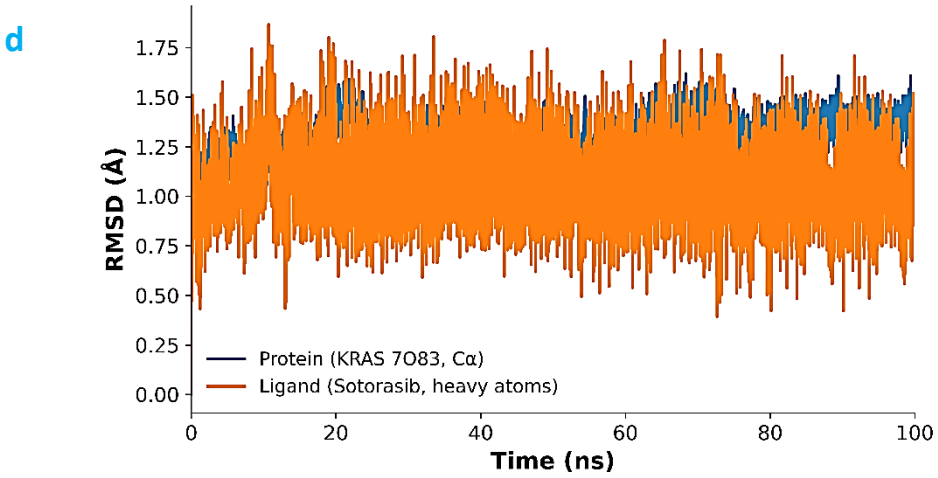

Figure 2. RMSD profiles of KRAS(G12C)–ligand complexes during 100-ns molecular dynamics simulations. (a) RMSD of KRAS(G12C) protein Cα atoms and C9 ligand heavy atoms in the 7O70 complex, (b) RMSD of KRAS(G12C) protein Cα atoms and sotorasib ligand heavy atoms in the 7O70 complex, (c) RMSD of KRAS(G12C) protein Cα atoms and C9 ligand heavy atoms in the 7O83 complex. And (d) RMSD of KRAS(G12C) protein Cα atoms and sotorasib ligand heavy atoms in the 7O83 complex. Root mean square deviation (RMSD) trajectories of protein backbone Cα atoms (blue) and ligand heavy atoms (orange) over 100 ns molecular dynamics simulations for KRAS(G12C) complexes with C9 (test compound) and sotorasib (control) across two KRAS conformational states (PDB IDs: 7O70 and 7O83). Protein Cα atoms were aligned structurally, and RMSD values were calculated with respect to the first frame. Protein RMSD is a measure of global backbone stability, and ligand RMSD is a measure of binding pose stability within the Switch-II pocket.

The RMSD trajectories of both the structural systems indicated that the protein backbone equilibrated at the early stage of the simulations and showed structural stability. The ligands displayed a consistent binding orientation in the KRAS(G12C) Switch-II pocket during the 100-ns simulation period.

3.4 Global compactness: radius of gyration (Rg)

The global structural compactness of KRAS(G12C) in the molecular dynamics simulations was computed using the radius of gyration (Rg), which is a measure of the mass-weighted distribution of atoms around the centre of mass of the protein. We used Rg analysis to determine the structural compactness or expansion of the KRAS backbone during the 100-ns simulations.

For the KRAS(G12C)–C9 complex, taken from the 7O70 structure, the Rg trajectory showed a short equilibration period in the first few nanoseconds and then stable fluctuations for the rest of the simulation. The Rg values varied between 14.9 Å and 15.2 Å, with a mean value of 15.08 ± 0.08 Å and, thus, the global compactness of the protein was stable during the trajectory (Figure 3a).

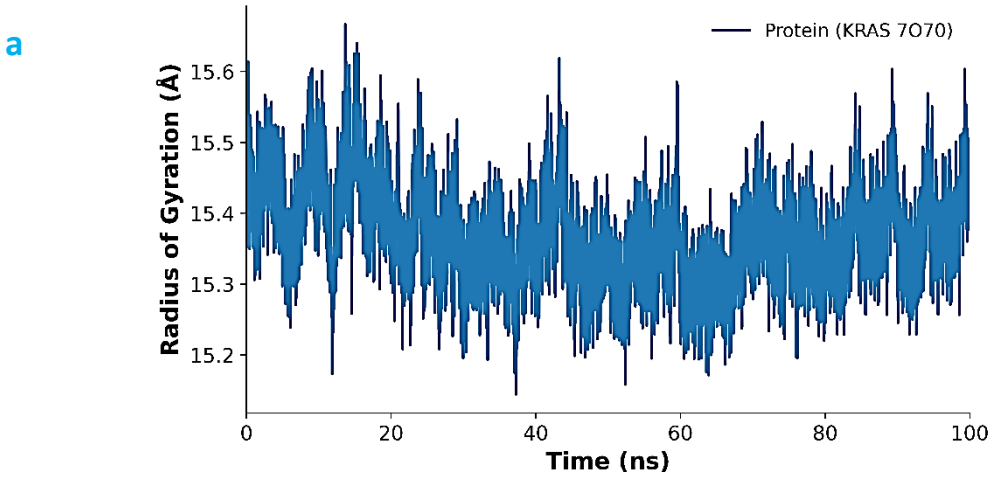

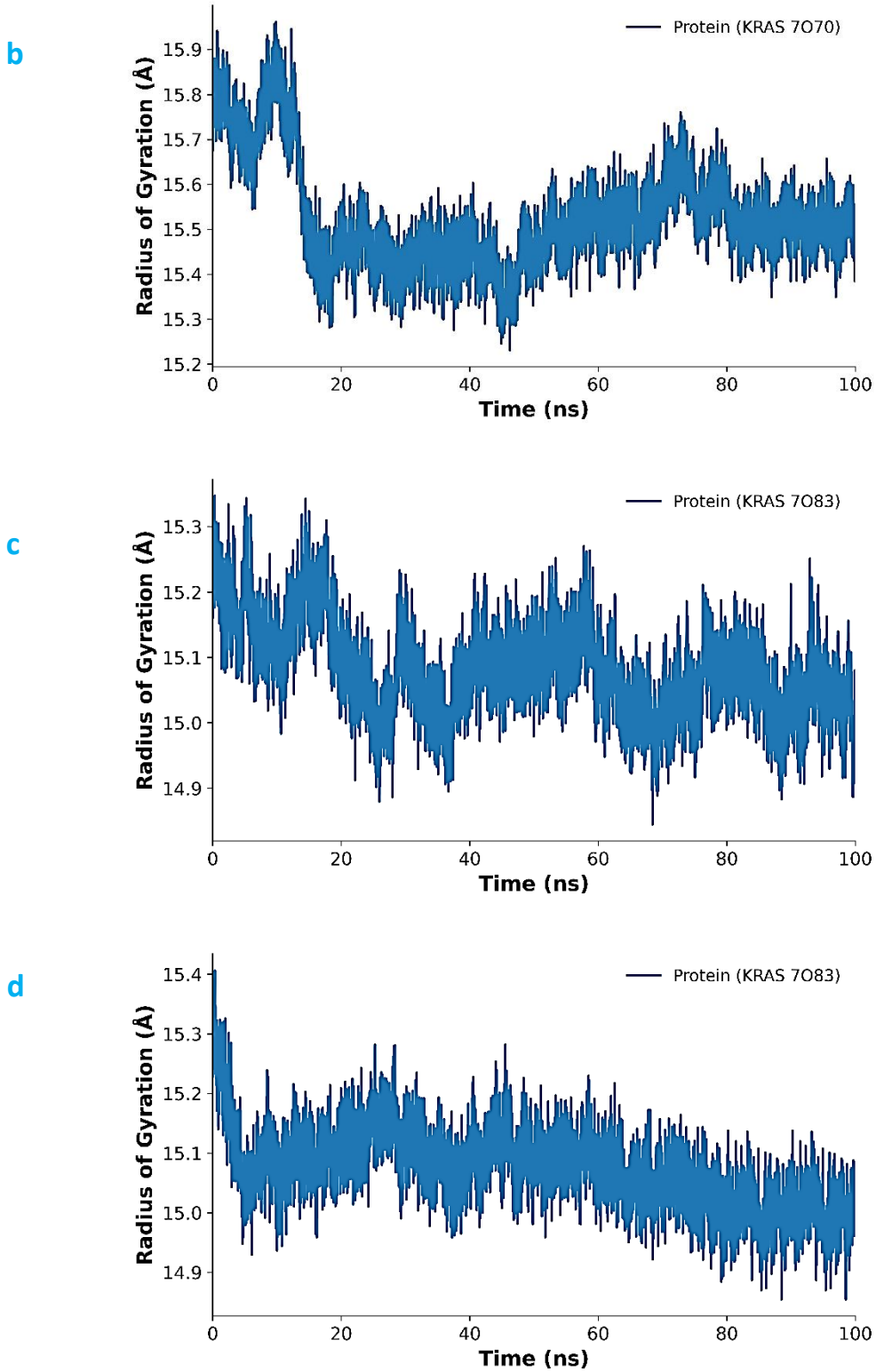

Figure 3. Radius of gyration (Rg) analysis of KRAS(G12C) complexes during 100-ns molecular dynamics simulations. Figure 3a–d. Time evolution of the radius of gyration (Rg) of KRAS(G12C) in complex with C9 (test compound) and sotorasib (control) across two KRAS conformational states. (a) KRAS(G12C)–C9 complex based on 7O70. (b) KRAS(G12C)–sotorasib complex based on 7O70. (c) KRAS(G12C)–C9 complex based on 7O83. (d) KRAS(G12C)–sotorasib complex based on 7O83. Radius of gyration (Rg) trajectories for KRAS(G12C) complexes calculated over 100 ns molecular dynamics simulations. Rg values were computed from protein backbone atoms to evaluate global structural compactness of the protein. Across all complexes, the Rg values fluctuate within narrow ranges without systematic drift, indicating that the overall fold and compactness of the KRAS protein remain stable during the simulations.

For the KRAS(G12C)–C9 complex, using the 7O70 structure, the Rg trajectory shows a short equilibration period in the first nanoseconds and then stable fluctuations during the rest of the simulation. The Rg values ranged narrowly from around 14.9–15.2 Å with an average of 15.08 ± 0.08 Å, which revealed the stable global compactness of the protein during the trajectory (Figure 3a).

For the KRAS(G12C)–sotorasib complex, the Rg profile for the 7O70 structure also exhibited stable behaviour after early equilibration. The Rg values varied from ~15.3 to 15.9 Å with an average value of 15.53 ± 0.13 Å over the simulation. However, no systematic increase or decrease in trajectory over time was found, although small fluctuations were observed (Figure 3b).

Likewise, the KRAS(G12C)–sotorasib complex in the 7O83 structure displayed stable Rg behaviour during the entire simulation. The values ranged from ~14.9 to 15.4 Å with an average of 15.08 ± 0.11 Å (Figure 3d). The trajectory did not show a progressive drift, suggesting that the KRAS(G12C) backbone maintained overall structural compactness during the simulation time.

3.5 Interaction energetics: ligand–protein interaction energy (LIE)

Furthermore, we examined the energetic stability of ligand binding to KRAS(G12C) by investigating the nonbonded ligand-protein interaction energies over 100 ns of molecular dynamics simulations. The interaction energy was decomposed into the electrostatic and van der Waals (vdW) contributions, and the total interaction energy was the sum of these contributions. These energy profiles shed light on the dominant forces that stabilise the ligand binding and whether the ligand-protein interactions are persistent during the trajectory.

In the 7O70 structure, the total interaction energy of the KRAS(G12C)–C9 complex was always negative throughout the trajectory with values ranging from about −55 to −75 kcal/mol and an average of approximately −65 kcal/mol. The largest contribution to stabilisation was van der Waals, which varied between −50 and −60 kcal/mol during the simulation. In contrast, the electrostatic part resulted in a smaller but constant interaction energy from −8 to −18 kcal/mol. In the short term, fluctuations were observed, but the overall energy profile was stable with no progressive drift to weaker interactions, suggesting persistent ligand-protein contacts between C9 and the binding pocket of KRAS(G12C) in the structural context of 7O70 (Figure 4a).

A similar energetic pattern was found for the KRAS(G12C)–sotorasib complex from the structure 7O70. The total interaction energy was in the range of approximately -58 to -72 kcal/mol with an average of approximately -64 kcal/mol over the trajectory. As observed for the C9 complex, the van der Waals interactions were the main stabilising component with values generally between − 48 and − 60 kcal/mol, while the electrostatic term was smaller in magnitude with values generally between − 8 and − 16 kcal/mol. The interaction energies were negative throughout the entire simulation, but they fluctuated transiently, demonstrating the stable energetic interactions of sotorasib with the KRAS(G12C) binding pocket in the 7O70 structural environment (Figure 4b).

The interaction energy profile of the KRAS(G12C)–C9 complex based on the structure 7O83 exhibited larger fluctuations compared to the system 7O70 and dynamic rearrangements in the binding pocket were reflected. The total interaction energy varied between approximately −40 and −10 kcal/mol throughout the simulation. As in the 7O70 system, the stabilising contribution was dominated by van der Waals interactions, with typical fluctuations in the range −30 to −10 kcal/mol, while the electrostatic component was relatively small, fluctuating between −8 and +2 kcal/mol. For about 75–85 ns a transient period was observed where the interaction strength was temporarily decreased. Both components of the energy approach zero before they become negative near the end of the trajectory. The interaction energy was variable with a dominant negative component indicating more dynamic but ongoing ligand-protein interactions for C9 in the 7O83 conformation of KRAS(G12C) (Figure 4c).

In contrast, the KRAS(G12C)–sotorasib complex with the 7O83 structure showed intermittent fluctuations in the interaction energy with total interaction energies in the range of approximately −35 to +5 kcal/mol over the entire trajectory. The van der Waals component was the main stabilising component, with a typical variation from -30 to -10 kcal/mol, while the electrostatic interactions were weak, with a typical variation from -5 to +2 kcal/mol. Longer times between ~20 and 80 ns showed interaction energies near 0 kcal/mol, suggesting a transient weakening of ligand-protein interactions during these times. In the last part of the simulation (~85–100 ns), more pronounced negative interaction energies re-emerged, indicative of the re-established van der Waals interactions between sotorasib and the KRAS(G12C) binding pocket (Figure 4d).

In general, the ligand-protein interaction energy profiles suggest that the van der Waals interactions are the main contributor to the stabilisation of the ligand binding in both structural conformations, whereas the electrostatic contribution is minor. In the 7O70 system, the C9 complex exhibited consistently strong negative interaction energies, and in the 7O83 system, sustained interactions, indicative of stable ligand binding throughout the simulated trajectories.

a

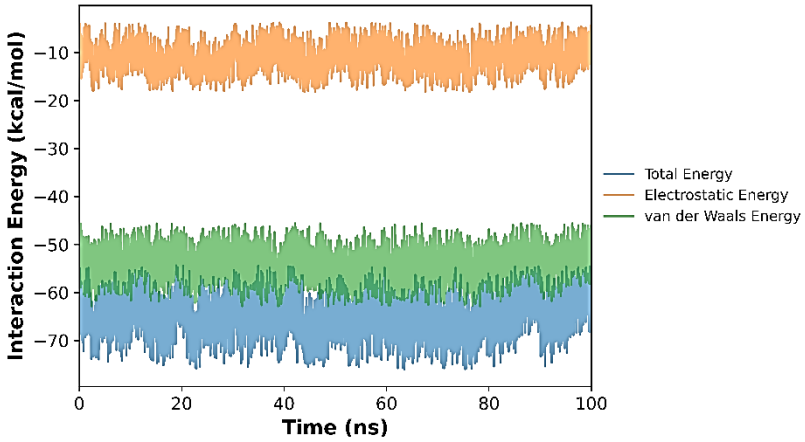
Interaction Energy (kcal/mol)
−10
−20
−30
−40
−50
−60
−70
0
20
40
60
80
100
Time (ns)
Total Energy
Electrostatic Energy
van der Waals Energy

b

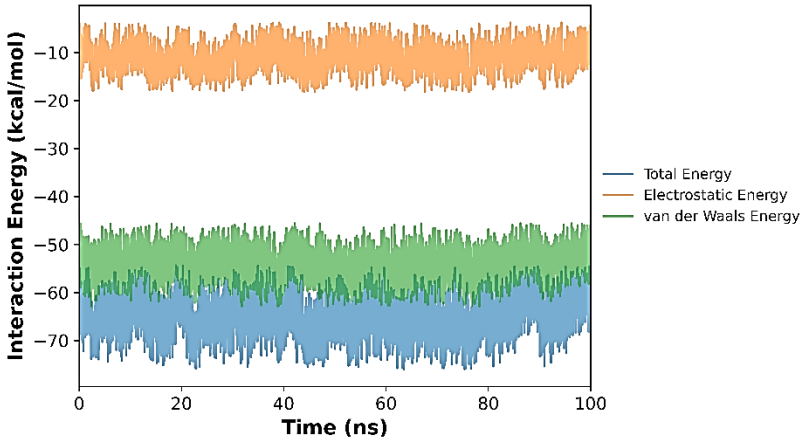
Interaction Energy (kcal/mol)
−10
−20
−30
−40
−50
−60
−70
0
20
40
60
80
100
Time (ns)
Total Energy
Electrostatic Energy
van der Waals Energy

c

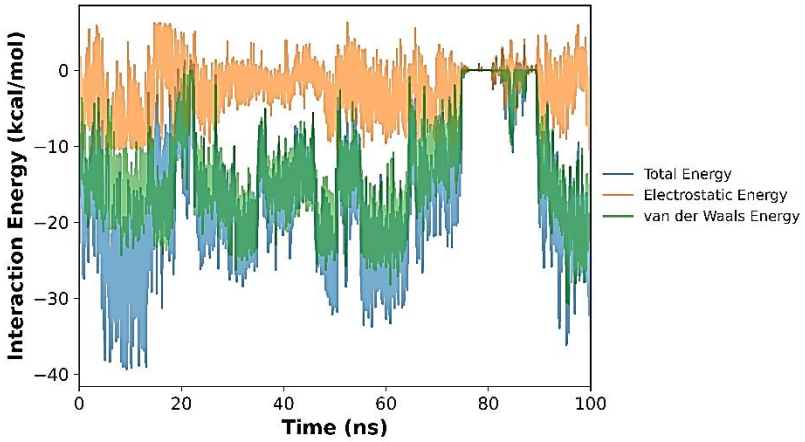
Interaction Energy (kcal/mol)
0
−10
−20
−30
−40
0
20
40
60
80
100
Time (ns)
Total Energy
Electrostatic Energy
van der Waals Energy

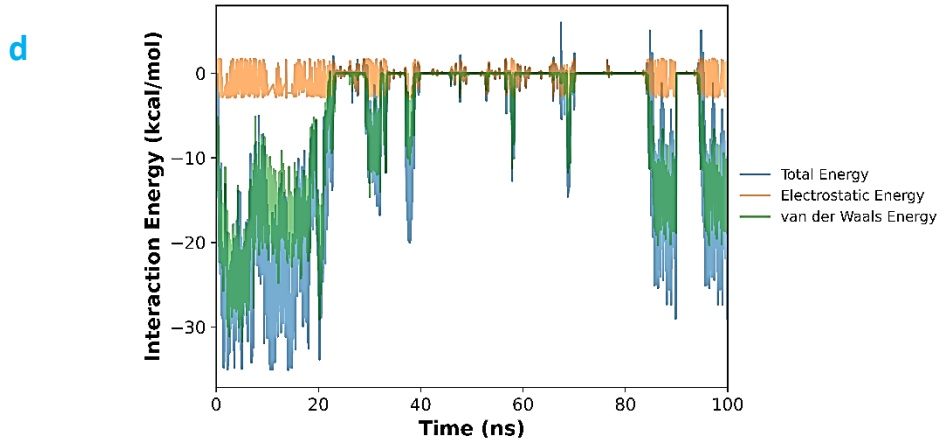

Figure 4. Time evolution of ligand–protein interaction energies during molecular dynamics simulations of KRAS(G12C) complexes. Time-resolved decomposition of ligand–protein interaction energies over the 100-ns molecular dynamics simulations for KRAS(G12C) complexes. The total interaction energy (blue) represents the sum of electrostatic (orange) and van der Waals (green) contributions. (a) KRAS(G12C)–C9 complex based on the 7O70 crystal structure. Strong negative interaction energies are consistent and dominated by van der Waals interactions. (b) KRAS(G12C)–sotorasib complex based on the 7O70 structure. Stable energetic interactions with similar vdW dominated stabilisation profile, (c) KRAS(G12C)–C9 complex based on the 7O83 structure, where larger fluctuations in interaction energy reflect dynamic rearrangements within the binding pocket while maintaining predominantly negative interaction energies and (d) KRAS(G12C)–sotorasib complex based on the 7O83 structure, displaying intermittent weakening of interactions during portions of the trajectory followed by recovery of stabilizing van der Waals contacts toward the later stages of the simulation.

4. DISCUSSION

4.1 Ligand–protein interaction networks across KRAS(G12C) conformations

KRAS mutations, in particular the G12C mutation, represent some of the most common oncogenic drivers in human cancers and have long been considered difficult pharmacological targets due to the protein's high affinity for GTP/GDP and the lack of deep druggable pockets on the protein surface. The discovery of the Switch-II pocket, which is adjacent to the mutated Cys12 residue, overturned the original research paradigm and established a platform for developing covalent inhibitors that can selectively bind to the inactive GDP-bound state of KRAS(G12C) (Moore et al., 2020; Anastasiou et al., 2024; Cuevas-Navarro et al., 2024). The first clinically approved inhibitor, sotorasib (AMG 510), showed that selective targets of this pocket can produce meaningful clinical responses in KRAS(G12C)-driven tumours, particularly non–small cell lung cancer (Anastasiou et al., 2024, Cuevas-Navarro, et al., 2024, Skoulidis et al., 2021). Nevertheless, the emergence of resistance mechanisms and heterogeneous clinical responses has increased the requirement for additional chemotypes that can engage the KRAS(G12C) pocket with alternative modes of interaction (Awad et al., 2021, Tanaka et al., 2021, Hofmann et al., 2022). In this work, we investigated the potential KRAS(G12C) inhibitor quinazoline derivative C9 through a combined ensemble docking with molecular dynamics (MD) simulation approach.

Through ensemble docking experiments, this study found that ligand C9 exhibited superior binding affinity compared to sotorasib across all tested conformations of KRAS(G12C). It can adapt to the structural variability of the Switch-II pocket. In the design of KRAS inhibitors, structural heterogeneity is a core factor that must be prioritised. The Switch-II region has rearrangements in conformation depending on the nucleotide state and the ligand engagement (Cuevas-Navarro et al., 2024; Hunter et al., 2015). Ensemble docking is thus an increasingly useful strategy for finding ligands that can maintain favourable interactions across multiple protein conformations rather than relying on a single static structure (Amaro et al., 2018). The fact that C9 showed higher predicted affinities for both the 7O70 and 7O83 structures indicates that the quinazoline scaffold can adapt to conformations within the pocket. This adaptability is important for KRAS inhibitors since the Switch-II region can undergo local structural plasticity that affects ligand orientation and binding stability (Hunter et al., 2015).

The analysis of the ligand–protein interaction networks shows that both C9 and reference inhibitor sotorasib bind to residues characteristic of the KRAS(G12C) Switch-II pocket, e.g., Cys12, Glu62, Arg68, Asp69, Asp92, Met72, His95, and Tyr96. These residues have been identified as determinants of ligand recognition in several structural and biochemical studies of KRAS inhibitors (Cuevas-Navarro et al., 2024; Fell et al., 2020). In particular, the proximity of ligands to Cys12 is a defining feature of many KRAS(G12C) inhibitors because the cysteine residue provides a unique opportunity for covalent targeting that is absent in wild-type KRAS (Anastasiou et al., 2024; Cuevas-Navarro et al., 2024). Although this study only evaluated ligand C9 based on non-covalent interaction

analyses. After a π-sulfur interaction involving the Cys12 residue was observed, it suggests that C9 is precisely localised within the Switch-II pocket, a property that can support the subsequent development of covalent and hybrid binding strategies.

Electrostatic interactions also appeared to play a prominent role in stabilising ligand binding. Both C9 and sotorasib exhibited π–cation interactions with Arg68 and complementary interactions with acidic residues such as Glu62 and Asp92. These residues line the interior of the Switch-II pocket and frequently contribute to ligand stabilisation via electrostatic or hydrogen-bonding interactions (Fell et al., 2020; Hansen et al., 2018). The electrostatic complementarity in this region has been shown to influence the selectivity and binding affinity of inhibitors, particularly for ligands with heteroaromatic scaffolds capable of forming π-interactions (Lu et al., 2016). These interactions are present in both complexes and suggest that the binding pocket creates a favourable electrostatic environment for stable ligand binding.

Furthermore, aromatic stacking interactions between Tyr96 and His95 were observed in several complexes. It has been shown that aromatic residues in the Switch-II pocket participate in ligand stabilisation through π–π stacking and hydrophobic packing interactions that help to retain the orientation of the ligand and limit conformational mobility in the binding site (Fell et al., 2020; Gentile et al., 2017). Such interactions are especially important for heterocyclic scaffolds such as quinazolines that often rely on aromatic contacts to anchor the ligand within the binding pockets of kinases or signalling proteins (Wang & Cole, 2014). Aromatic interactions with C9 Tyr96 and His95 indicate that the aromatic framework of the ligand is well suited to stabilise interactions within the KRAS binding cavity.

Hydrophobic contacts also facilitated further ligand stabilisation in the pocket. The residues Val9, Ala11, Met72, and Pro34 formed alkyl or π-alkyl interactions with the ligand scaffolds, indicating that hydrophobic packing is critical for ligand accommodation. The KRAS Switch-II pocket is lined with several nonpolar residues that favour ligand burial and solvent exclusion; hence, hydrophobic interactions are known to be critical determinants of binding affinity (Cuevas-Navarro et al., 2024; Baines et al., 2011). We thus find that the multiple identified hydrophobic contacts for both ligands are consistent with previously reported structural features of KRAS inhibitor binding.

Together, the docking and interaction analyses suggest that C9 can bind the KRAS(G12C) binding pocket via a combination of electrostatic, aromatic and hydrophobic interactions similar to those observed for clinically validated inhibitors. Importantly, the fact that C9 maintains favourable binding scores and interaction patterns in two structurally different KRAS conformations suggests that the ligand scaffold may have some conformational adaptability, which is a favourable characteristic for inhibitors targeting flexible protein regions, such as the Switch-II loop.

Nonetheless, several limitations should be noted. Docking and molecular dynamics simulations are powerful tools to get insights into possible binding mechanisms, but they are unable to fully mimic the complexity of cellular environments or account for conformational transitions that take place on long timescales. Furthermore, the present work mainly focused on noncovalent interactions, whereas some clinically successful KRAS(G12C) inhibitors such as sotorasib are based on covalent modification of Cys12 to provide long-lasting inhibition (Anastasiou et al., 2024; Cuevas-Navarro et al., 2024). Future work should therefore tackle the question of whether the C9 scaffold can be tuned to accommodate electrophilic warheads covalently engaging Cys12 while maintaining the favourable noncovalent interactions seen in the present simulations.

In general, the results presented here provide in silico support to the quinazoline derivative C9 as a potential scaffold for the inhibition of KRAS(G12C). By combining ensemble docking and interaction network analysis across different KRAS conformations, this study identifies crucial molecular determinants that could guide the future optimisation of C9 derivatives. Experimental validation that the predicted interactions result in functional KRAS inhibition within biological systems necessitates biochemical binding assays, cellular signalling studies, and structure-guided medicinal chemistry optimisation.

4.2 Stability of KRAS(G12C)–ligand complexes revealed by RMSD trajectories

The dynamic stability of the KRAS(G12C)–ligand complexes was further emphasised by molecular dynamics simulations, extending beyond the static interaction networks seen from docking. Root mean square deviation (RMSD), which is the deviation of the structure from the initial conformation during the simulation, was used to assess the structural stability of the protein-ligand complex (Hollingsworth & Dror, 2018; Hospital et al., 2015). The RMSD profiles of the protein backbone (Cα atoms) and ligand heavy atoms in the present study showed that all complexes reached equilibrium at the initial stages of the 100-ns simulations and maintained stable trajectories thereafter.

The protein backbone RMSD for the KRAS(G12C)–C9 complex in the 7O70 structure remained relatively low throughout the trajectory, fluctuating between ~1.3 and 1.7 Å. Such small deviations are generally suggestive of a structurally stable protein fold during simulation (Hollingsworth & Dror, 2018). Even lower ligand RMSD values were observed from 0.5 to 1.1 Å, indicating the ligand adopted a very stable binding orientation inside the Switch-II pocket. The small ligand displacement during the trajectory suggests a strong retention of the docked pose and little structural rearrangement in the binding site.

In contrast, the RMSD for the protein backbone in the KRAS(G12C)–sotorasib complex in 7O70 had a slightly higher range. In the early stage of the simulation, this indicator first increased, then stabilised at 2.3–3.1 Å, which indicates that the protein completed a mild structural adjustment. Ligand RMSD values were 1.6–2.4 Å, suggesting moderate ligand mobility during the initial equilibration phase before the ligand adopted a stable binding pose. Such early fluctuations are commonly seen in MD simulations and are often a sign of local relaxation of the docking pose into the binding pocket (Hospital et al., 2015; Karplus & McCammon, 2002).

Simulations based on the 7O83 crystal structure showed a similar pattern of stability, although overall fluctuations were somewhat smaller. In the KRAS(G12C)–C9 complex, the protein RMSD stabilised around ~1.3–1.6 Å after equilibration, while the ligand RMSD values remained in the range of 0.8–1.3 Å. These values suggest that the ligand remained tightly bound and consistently oriented in the Switch-II pocket throughout the simulation. Likewise, the KRAS(G12C)–sotorasib complex in the 7O83 structure displayed stable RMSD trajectories with protein RMSD values fluctuating between 1.3 and 1.5 Å and ligand RMSD values ranging between 0.9 and 1.4 Å. These small deviations indicate that the protein backbone and the ligand pose held up structurally over the entire simulation window.

Overall, the RMSD trajectories confirm that all KRAS(G12C)–ligand complexes attained a dynamic equilibrium relatively early in the simulations and remained in stable conformations throughout the 100-ns trajectories. Importantly, the C9 complexes showed low ligand RMSD values throughout, suggesting that they stayed bound in the Switch-II pocket across both KRAS conformations. These observations are consistent with the docking results and suggest that the quinazoline scaffold of C9 can adopt a stable binding pose similar to the clinically validated inhibitor sotorasib. The convergence of the RMSD trajectories thus provides further computational evidence of the structural compatibility of C9 with the KRAS(G12C) binding cavity.

4.3 Stability of KRAS(G12C) global fold assessed by radius of gyration

The radius of gyration (Rg) is another measure of how atomic mass is distributed around the centre of mass of the protein and gives an idea of the global structural compactness of the protein during the simulation. In molecular dynamics simulations, Rg is often used to evaluate whether a protein undergoes a large-scale structural expansion, collapse, or unfolding during a simulation (Dror et al., 2012; Padhi et al., 2022). In the present study, we used Rg trajectories to assess whether ligand binding affected the global architecture of KRAS(G12C) between the two structural conformations examined.

For the KRAS(G12C)–C9 complex from structure 7O70, the Rg profile indicated a short equilibration period in the beginning of the simulation and stable fluctuations for the rest of the trajectory. The Rg values were determined to be in the narrow range of about 14.9–15.2 Å, with a mean value of 15.08 ± 0.08 Å. Such small variations imply that the global fold of KRAS was structurally compact during the entire simulation and that ligand binding did not induce large-scale conformational expansion.

Similar was the behaviour of the KRAS(G12C)–sotorasib complex (7O70 structure), where the Rg trajectory was stabilised after the initial equilibration phase. The Rg values ranged from 15.3 to 15.9 Å with an average value of 15.53 ± 0.13 Å. The mean Rg was slightly increased over the C9 complex, but the lack of progressive drift over the trajectory indicates that overall protein architecture was stable during ligand binding.

Likewise, simulations of KRAS(G12C) with the 7O83 structural fold retained global compactness of KRAS(G12C). The Rg values for the KRAS(G12C)–C9 complex fluctuated between 14.9 and 15.3 Å, with an average value of 15.08 ± 0.10 Å, indicating a stable structural compactness during the trajectory. Similarly, the KRAS(G12C)–sotorasib complex from 7O83 showed stable Rg values between 14.9 and 15.4 Å, with an average of 15.08 ± 0.11 Å. No systematic change of Rg was observed along the simulation time, indicating that the global fold of KRAS was maintained in the presence of either ligand.

Together, the Rg trajectories demonstrate that neither conformational state of the KRAS(G12C) backbone showed structural expansion or destabilisation upon ligand binding. The stable Rg values for all the complexes suggested that the overall compactness of KRAS was not significantly altered during the 100 ns molecular dynamics simulations, which further confirmed the structural stability of the simulated systems.

4.4 Interaction energetics: ligand–protein interaction energy (LIE)

Understanding the energetic determinants of ligand binding is important for evaluating the stability and persistence of protein ligand complexes in molecular dynamics simulations. In particular, decomposing interaction energies into electrostatic and van der Waals (vdW) contributions provides insight into the dominant forces stabilising ligand binding in protein pockets. Such analyses are widely used in molecular simulation studies to characterise binding energetics and to identify if ligand-protein contacts are energetically favourable over time (Padhi et al., 2022; Åqvist et al., 1994; Genheden & Ryde, 2015). In the present work, we followed the non-bonded interaction energies between the ligands and KRAS(G12C) during the 100-ns simulations to assess the stability of ligand binding in the Switch-II pocket.

The average total interaction energy for the KRAS(G12C)–C9 complex with the 7O70 structure was negative throughout the simulation trajectory, ranging from about −55 to −75 kcal/mol, with an average of about −65 kcal/mol. The largest stabilising contribution came from the van der Waals contribution, which typically fell in the range of -50 to -60 kcal/mol. This indicates a significant contribution of hydrophobic packing and dispersion interactions to stabilise the ligand within the binding cavity. While electrostatic interactions make a small contribution, they cannot be ignored, from −8 to −18 kcal/mol. The lack of any progressive energetic drift suggested that C9 was in stable nonbonded contacts with KRAS(G12C) in the structural context of 7O70, albeit with transient fluctuations.

The KRAS(G12C)–sotorasib complex in the 7O70 structure exhibited a similar energetic profile. The total interaction energy fluctuated in a narrow range from about −58 to −72 kcal/mol with an average value of about −64 kcal/mol. As in the C9 system, the dominant contribution to the stabilisation was the van der Waals interactions, typically between -48 and -60 kcal/mol, whereas the electrostatic contribution was modest, typically between -8 and -16 kcal/mol. The negative interaction energies present throughout the trajectory show that sotorasib also established stable energy interactions with the binding pocket of KRAS(G12C) in this conformation.

The interaction energy profile of the KRAS(G12C)–C9 complex from the 7O83 structure showed more pronounced fluctuations, indicating a higher degree of conformational flexibility of the binding pocket. Total interaction energy fluctuated between around −40 and −10 kcal/mol during the course of the simulation. In the 7O70 system, van der Waals forces were the dominant stabilising factor for ligand-protein binding, with energy values ranging from -30 to -10 kcal/mol; electrostatic forces were smaller, ranging from -8 to +2 kcal/mol. We observe a transient from 75 to 85 ns where the interactions are weakened, and both components tend towards near-neutral values before returning to negative values near the end of the trajectory. Despite such fluctuations, the overall energy profile was mostly negative, which proves that their interaction persists continuously and is dynamically regulated by ligand-protein interactions for C9 in the 7O83 conformational state.

By contrast, the 7O83 structure-based KRAS(G12C)–sotorasib complex exhibited more fluctuation in the interaction energy. Total interaction energy was in the range of about −35 to +5 kcal/mol during the trajectory. Again, the main stabilising contribution was from the van der Waals component, which was usually in the range −30 to −10 kcal/mol, and electrostatic interactions were weak, usually in the range −5 to +2 kcal/mol. In long periods of time, from about 20 to 80 ns, the interaction energies were close to 0 kcal/mol, meaning ligand–protein contacts were temporarily weakened. In the late phase of the simulation (~85-100 ns), however, the negative interaction energies re-appeared more strongly, indicating a renewed stabilisation by van der Waals interactions between sotorasib and the KRAS(G12C) binding pocket.

5. CONCLUSION

In conclusion, this study demonstrates that the quinazoline derivative C9 is a credible and structurally stable candidate for targeting mutant KRAS(G12C). In ensemble docking against different conformations of KRAS(G12C), C9 consistently yielded more favourable predicted binding affinities than the reference inhibitor sotorasib, and interaction mapping displayed sustained engagement with key residues of the Switch-II pocket including Cys12, Glu62, Arg68, Asp69, Asp92, Met72, His95 and Tyr96. These results were also supported by molecular dynamics simulations, which showed stability of the protein backbone, persistence of ligand poses, maintenance of global compactness, and mostly favourable ligand-protein interaction energies, with van der Waals contacts as the main stabilising force. Collectively, these data suggest that C9 is capable of engaging in productive, long-lived interactions with the KRAS(G12C) binding pocket in more than one conformational state, consistent with its potential as a scaffold for future lead optimisation. Experimental validation and structure-guided medicinal chemistry optimisation will be required to confirm its inhibitory activity and progress its development as a next-generation KRAS(G12C)-targeted therapeutic candidate.

Acknowledgements
The authors sincerely thank and acknowledge the researchers whose published work provided evidence that facilitated the completion of this systematic review and meta-analysis.

Author Contributions:
Stephen Adebayo Osasan and George Oche Ambrose contributed equally to the conception and design of the study, data analysis and interpretation, and manuscript preparation. Olusola Daramola, Oluwafemi Ayodele Adefolalu, Alzahrani A. Hind, Mohammad Alshehri Jawaher, Wisdom Onuche Ibrahim and Olanrewaju I. Ajetunmobi interpreted the data and revised the manuscript critically. All authors have read and approved the final manuscript and are accountable for the integrity of the work.

Ethical Approval
Not applicable. This article does not contain any studies with human participants or animals performed by any of the authors.

Informed Consent
Not applicable.

Conflicts of interests
The authors declare that they have no conflicts of interest, competing financial interests or personal relationships that could have influenced the work reported in this paper.

Funding
This research did not receive any external funding like specific grant from funding agencies in the public, commercial, or nonprofit sectors.

Data and materials availability
All data associated with this study will be available upon reasonable request to the corresponding author.

REFERENCES

1. Amaro RE, Baudry J, Chodera J, Demir Ö, McCammon JA, Miao Y, Smith JC. Ensemble docking in drug discovery. Biophys J 2018;114(10):2271-2278. doi: 10.1016/j.bpj.2018.02.038.
2. Anastasiou P, Moore C, Rana S, Tomaschko M, Pillsbury CE, de Castro A, Boumelha J, Mugarza E, de Carné Trécesson S, Mikolajczak A, Blaj C, Goldstone R, Smith JAM, Quintana E, Molina-Arcas M, Downward J. Combining RAS(ON) G12C-selective inhibitor with SHP2 inhibition sensitises lung tumours to immune checkpoint blockade. Nat Commun 2024; 15(1):8146. doi: 10.1038/s41467-024-52324-3.
3. Åqvist J, Medina C, Samuelsson JE. A new method for predicting binding affinity in computer-aided drug design. Protein Eng 1994;7(3):385-391. doi: 10.1093/protein/7.3.385.
4. Awad MM, Liu S, Rybkin II, Arbour KC, Dilly J, Zhu VW, Johnson ML, Heist RS, Patil T, Riely GJ, Jacobson JO, Yang X, Persky NS, Root DE, Lowder KE, Feng H, Zhang SS, Haigis KM, Hung YP, Sholl LM, Wolpin BM, Wiese J, Christiansen J, Lee J, Schrock AB, Lim LP, Garg K, Li M, Engstrom LD, Waters L, Lawson JD, Olson P, Lito P, Ou SHI, Christensen JG, Jänne PA, Aguirre AJ. Acquired resistance to KRASG12C inhibition in cancer. N Engl J Med 2021;384(25):2382-2393. doi: 10.1056/NEJMoa2105281.
5. Baines AT, Xu D, Der CJ. Inhibition of Ras for cancer treatment: the search continues. Future Med Chem 2011;3(14): 1787-1808. doi: 10.4155/fmc.11.121.
6. Canon J, Rex K, Saiki AY, Mohr C, Cooke K, Bagal D, Gaida K, Holt T, Knutson CG, Koppada N, Lanman BA, Werner J, Rapaport AS, San Miguel T, Ortiz R, Osgood T, Sun JR, Zhu X, McCarter JD, Volak LP, Houk BE, Fakih MG, O'Neil BH, Price TJ, Falchook GS, Desai J, Kuo J, Govindan R, Hong DS, Ouyang W, Henary H, Arvedson T, Cee VJ, Lipford JR. The clinical KRAS(G12C) inhibitor AMG 510 drives anti-tumour immunity. Nature 2019;575(7781):217-223. doi: 10.1038/s41586-019-1694-1.
7. Cherkasov A, Muratov EN, Fourches D, Varnek A, Baskin II, Cronin M, Dearden J, Gramatica P, Martin YC, Todeschini R, Consonni V, Kuz'min VE, Cramer R, Benigni R, Yang C, Rathman J, Terfloth L, Gasteiger J, Richard A, Tropsha A. QSAR modeling: where have you been? Where are you going

to? J Med Chem 2014;57(12):4977-5010. doi: 10.1021/jm4004285.
8. Cox AD, Fesik SW, Kimmelman AC, Luo J, Der CJ. Drugging the undruggable RAS: mission possible? Nat Rev Drug Discov 2014;13(11):828-851. doi: 10.1038/nrd4389.
9. Cuevas-Navarro A, Pourfarjam Y, Hu F, Rodriguez DJ, Vides A, Sang B, Fan S, Goldgur Y, de Stanchina E, Lito P. Pharmacological restoration of GTP hydrolysis by mutant RAS. Nature 2025;637(8044):224-229. doi: 10.1038/s41586-024-08283-2.
10. Dror RO, Dirks RM, Grossman JP, Xu H, Shaw DE. Biomolecular simulation: a computational microscope for molecular biology. Annu Rev Biophys 2012;41:429-452. doi: 10.1146/annurev-biophys-042910-155245.
11. Fell JB, Fischer JP, Baer BR, Blake JF, Bouhana K, Briere DM, Brown KD, Burgess LE, Burns AC, Burkard MR, Chiang H, Chicarelli MJ, Cook AW, Gaudino JJ, Hallin J, Hanson L, Hartley DP, Hicken EJ, Hingorani GP, Hinklin RJ, Mejia MJ, Olson P, Otten JN, Rhodes SP, Rodriguez ME, Savechenkov P, Smith DJ, Sudhakar N, Sullivan FX, Tang TP, Vigers GP, Wollenberg L, Christensen JG, Marx MA. Identification of the clinical development candidate MRTX849, a covalent KRASG12C inhibitor for the treatment of cancer. J Med Chem 2020;63(13):6679-6693. doi: 10.1021/acs.jmedchem.9b02052.
12. Genheden S, Ryde U. The MM/PBSA and MM/GBSA methods to estimate ligand-binding affinities. Expert Opin Drug Discov 2015;10(5):449-461. doi: 10.1517/17460441.2015.1032936.
13. Gentile DR, Rathinaswamy MK, Jenkins ML, Moss SM, Siempelkamp BD, Renslo AR, Burke JE, Shokat KM. Ras binder induces a modified switch-II pocket in GTP and GDP states. Cell Chem Biol 2017;24(12):1455-1466.e14. doi: 10.1016/j.chembiol.2017.08.025.
14. Hansen R, Peters U, Babbar A, Chen Y, Feng J, Janes MR, Li LS, Ren P, Liu Y, Zarrinkar PP. The reactivity-driven biochemical mechanism of covalent KRASG12C inhibitors. Nat Struct Mol Biol 2018;25(6):454-462. doi: 10.1038/s41594-018-0061-5.
15. Hofmann MH, Gerlach D, Misale S, Petronczki M, Kraut N. Expanding the reach of precision oncology by drugging all KRAS mutants. Cancer Discov 2022;12(4):924-937. doi: 10.1158/2159-8290.CD-21-1331.
16. Hollingsworth SA, Dror RO. Molecular dynamics simulation for all. Neuron 2018;99(6):1129-1143. doi: 10.1016/j.neuron.2018.08.011.
17. Hospital A, Goñi JR, Orozco M, Gelpí JL. Molecular dynamics simulations: advances and applications. Adv Appl Bioinform Chem 2015;8:37-47. doi: 10.2147/AABC.S70333.
18. Hunter JC, Manandhar A, Carrasco MA, Gurbani D, Gondi S, Westover KD. Biochemical and structural analysis of common cancer-associated KRAS mutations. Mol Cancer Res 2015;13(9):1325-1335. doi: 10.1158/1541-7786.MCR-15-0203.
19. Karplus M, McCammon JA. Molecular dynamics simulations of biomolecules. Nat Struct Biol 2002;9(9):646-652. doi: 10.1038/nsb0902-646.
20. Lanman BA, Allen JR, Allen JG, Amegadzie AK, Ashton KS, Booker SK, Chen JJ, Chen N, Frohn MJ, Goodman G, Kopecky DJ, Liu L, Lopez P, Low JD, Ma V, Minatti AE, Nguyen TT, Nishimura N, Pickrell AJ, Reed AB, Shin Y, Siegmund AC, Tamayo NA, Tegley CM, Walton MC, Wang HL, Wurz RP, Xue M, Yang KC, Achanta P, Bartberger MD, Canon J, Hollis LS, McCarter JD, Mohr C, Rex K, Saiki AY, San Miguel T, Volak LP, Wang KH, Whittington DA, Zech SG, Lipford JR, Cee VJ. Discovery of a covalent inhibitor of KRASG12C (AMG 510) for the treatment of solid tumors. J Med Chem 2020;63(1):52-65. doi: 10.1021/acs.jmedchem.9b01180.
21. Lu S, Jang H, Gu S, Zhang J, Nussinov R. Drugging Ras GTPase: a comprehensive mechanistic and signaling structural view. Chem Soc Rev 2016;45(18):4929-4952. doi: 10.1039/C5CS00911A.
22. Moore AR, Rosenberg SC, McCormick F, Malek S. RAS-targeted therapies: is the undruggable drugged? Nat Rev Drug Discov 2020;19(8):533-552. doi: 10.1038/s41573-020-0068-6.
23. Ostrem JM, Peters U, Sos ML, Wells JA, Shokat KM. K-Ras(G12C) inhibitors allosterically control GTP affinity and effector interactions. Nature 2013;503(7477):548-551. doi: 10.1038/nature12796.
24. Padhi AK, Janežič M, Zhang KYJ. Molecular dynamics simulations: principles, methods, and applications in protein conformational dynamics. In: Tripathi T, Dubey VK, editors. Advances in Protein Molecular and Structural Biology Methods. 1st ed. Cambridge (MA): Academic Press; 2022. p. 439-454. doi: 10.1016/B978-0-323-90264-9.00026-X.
25. Pylayeva-Gupta Y, Grabocka E, Bar-Sagi D. RAS oncogenes: weaving a tumorigenic web. Nat Rev Cancer 2011;11(11):761-774. doi: 10.1038/nrc3106.
26. Skoulidis F, Li BT, Dy GK, Price TJ, Falchook GS, Wolf J, Italiano A, Schuler M, Borghaei H, Barlesi F, Kato T, Curioni-Fontecedro A, Sacher A, Spira A, Ramalingam SS, Takahashi T, Besse B, Anderson A, Ang A, Tran Q, Mather O, Henary H, Ngarmchamnanrith G, Friberg G, Velcheti V, Govindan R. Sotorasib for lung cancers with KRAS p.G12C mutation. N Engl J Med 2021;384(25):2371-2381. doi: 10.1056/NEJMoa2103695.

27. Stephen Adebayo O, Oche Ambrose G, Olusola D, Oluwafemi A, Alzahrani HA, Hasan A. QSAR-guided discovery of novel KRAS inhibitors for lung cancer therapy. Front Bioinform 2025;5:1663846. doi: 10.3389/fbinf.2025.1663846.
28. Sung H, Ferlay J, Siegel RL, Laversanne M, Soerjomataram I, Jemal A, Bray F. Global cancer statistics 2020: GLOBOCAN estimates of incidence and mortality worldwide for 36 cancers in 185 countries. CA Cancer J Clin 2021;71(3):209-249. doi: 10.3322/caac.21660.
29. Tanaka N, Lin JJ, Li C, Ryan MB, Zhang J, Kiedrowski LA, Michel AG, Syed MU, Fella KA, Sakhi M, Baiev I, Juric D, Gainor JF, Klempner SJ, Lennerz JK, Siravegna G, Bar-Peled L, Hata AN, Heist RS, Corcoran RB. Clinical acquired resistance to KRASG12C inhibition through a novel KRAS switch-II pocket mutation and polyclonal alterations converging on RAS-MAPK reactivation. Cancer Discov 2021;11(8):1913-1922. doi: 10.1158/2159-8290.CD-21-0365.
30. Todeschini R, Consonni V. Molecular descriptors for chemoinformatics: Volume I: alphabetical listing; Volume II: appendices, references. 2nd rev enlarged ed. Methods and Principles in Medicinal Chemistry, vol. 41. Weinheim: Wiley-VCH; 2009. doi: 10.1002/9783527628766. Print ISBN: 978-3-527-31852-0; online ISBN: 978-3-527-62876-6.
31. Tropsha A. Best practices for QSAR model development, validation, and exploitation. Mol Inform 2010;29(6-7):476-488. doi: 10.1002/minf.201000061.
32. Wang Z, Cole PA. Catalytic mechanisms and regulation of protein kinases. Methods Enzymol 2014;548:1-21. doi: 10.1016/B978-0-12-397918-6.00001-X.
33. Westover KD, Jänne PA, Gray NS. Progress on covalent inhibition of KRASG12C. Cancer Discov 2016;6(3):233-234. doi: 10.1158/2159-8290.CD-16-0092.